Korean J. Chem. Eng., 35(2), 535-547 (2018)
DOI: 10.1007/s11814-017-0283-y

pISSN: 0256-1115
eISSN: 1975-7220

Adsorptive separation of carbon dioxide from flue gas using mesoporous MCM-41: A molecular simulation study

Kishant Kumar and Amit Kumar†

Department of Chemical Engineering, Indian Institute of Technology Guwahati, Guwahati, Assam 781039, India
(*Received 5 July 2017 • accepted 7 October 2017*)

Abstract−Realistic molecular models of MCM-41 have been developed and used for studying the separation of carbon dioxide from flue gas mixtures using grand canonical Monte Carlo simulations. The simulated X-ray diffraction pattern and surface area of the models are in good agreement with experimental results reported in literature. Adsorption of pure carbon dioxide was studied on the three different models at two different temperatures, 273.2 K and 303.2 K. Isosteric heats of adsorption of CO_2 calculated from the simulations were in the range 20-25 kJ/mol, which matches well with reported experimental values. The simulated CO_2 adsorption isotherms showed good agreement with experimental isotherms at both the temperatures for two of the models, which were selected for further mixture adsorption studies. Binary CO_2/N_2 adsorption simulations were performed at different bulk gas compositions, and the selectivities of CO_2 over N_2 were observed to be in the range 4-10. Further studies on adsorption of ternary and quaternary bulk gas mixtures containing water vapor and O_2 in addition to CO_2 and N_2 did not reveal any significant effect on CO_2 adsorption and CO_2-N_2 selectivity.

Keywords: Mesoporous Silica MCM-41, Molecular Modeling, Multicomponent Adsorption, CO_2/N_2 Separation, Grand Canonical Monte Carlo Simulation

INTRODUCTION

Increased consumption of carbon-containing fossil fuels to meet the rising demands in the power generation and transportation sector has led to increased emission of carbon dioxide in the atmosphere. Rise in the atmospheric concentration of carbon dioxide is believed to play a significant role in global warming through the greenhouse effect. Existing amine-based carbon capture technology is expensive and energy intensive, and is prohibitive when applied to large scale power plants, where the emission rates of CO_2 gas can be as high as 40 tons per minute [1]. Composition of the flue gas from the power plants depends upon the design of the power plants and source of the fuel used in the power plants such as natural gas and coal (see Table 1).

The important technologies that can be used for separation of carbon dioxide from flue gas are absorption, adsorption and membrane gas separation. Absorption using aqueous amine solutions is energy-intensive due to the large energy required for amine regeneration. Adsorptive separation of CO_2 using porous materials such as zeolites, mesoporous silicas, metal organic frameworks, and porous carbons is an attractive alternative to conventional amine scrubbing due to lower regeneration energy requirements. The surface area, pore texture, and pore size distribution of an adsorbent play a vital role in effective and efficient separation. The M41S family of mesoporous silica materials, discovered by researchers at Mobil Corporation in 1992, have large pores, uniform pore size and structure, and high surface area. MCM-41 belongs to M41S family of mesoporous silica materials and possesses high surface area, tunable pore size (by varying chain length of the surfactant during synthesis), uniformly aligned, ordered hexagonal arrangement of cylindrical pores, and considerable surface silanol groups. The surface area and pore volume are typically in the range of 700-1,500 m^2/g, and 0.7-1.0 cm^3/g respectively [2-4]. The pore size of MCM-41 is highly tunable and ranges from 15-100 Å. The pore walls consist of disordered network of siloxane bridges having skeletal density of 2.2-2.4 g/cm^3 [2]. These remarkable features of MCM-41 make it suitable for applications such as catalysis, gas adsorption and separation, and drug delivery.

Table 1. Typical composition of flue gas from coal-based and natural gas-based power plants (data taken from ref. [1])

Gas	Coal-based (in mbar)	Natural gas-based (in mbar)
CO_2	120-150	30-50
N_2	750-800	740-800
H_2O	50-140	70-100

MCM-41 was first synthesized by Kresge et al. [4] using aluminosilicate gels in the presence of surfactants having ordered array of pores arranged in hexagonal fashion with pore size in the range of 16 Å-100 Å. BET surface area and pore volume were found to be ≥1,000 m^2/g and 0.7-1.2 cm^3/g, respectively [4]. Zhaohua et al. [5] prepared aluminosilicate molecular sieves by following a synthesis procedure similar to that used for MCM-41. Two different raw materials, Catapal alumina or sodium aluminate and aluminum sulfate, were used as aluminum source to achieve 6- and 4-coordination number of aluminum, respectively. They showed through

†To whom correspondence should be addressed.
E-mail: amitkumar@iitg.ernet.in

XRD analysis and TEM images that hexagonal mesopore arrangement ceases to exist on increasing Si/Al ratio in the solid wall of the pore. They also confirmed that calcination at 550 °C for 24 hours enhances the mesopore formation. Catalytic activity of pure MCM-41 can be enhanced by substituting the silicon sites in the pore walls of MCM-41 with metal atoms. For example, Placidus et al. [6] modified pure MCM-41 by substituting silicon sites with Fe metal to obtain Fe-MCM-41, which was used as a catalyst for the production of carbon nanotubes by acetylene pyrolysis.

Yun et al. [7] studied the adsorption of methane, ethane and their binary mixtures on MCM-41 through molecular simulation using a simple model for cylindrical MCM-41 pores. He and Seaton [2,3] conducted molecular simulation study of pure gas and mixture adsorption behavior of methane, ethane and carbon dioxide in MCM-41 using the same simple model. This model of MCM-41 consists of three concentric, cylindrical layers of oxygen atoms made infinitely long by applying periodic boundary condition in the axial direction of the cylinders. The simple model represented a single, isolated pore and was not a very realistic representation of the hexagonally arranged pore network observed in real MCM-41. Zhuo et al. [8] performed molecular simulation studies on binary adsorption of CO_2/N_2 mixtures in mimetic MCM-41 models at representative flue gas composition, but did not consider the effect of the presence of other gases such as water vapor in the flue gas. Builes and Vega [9] investigated the adsorption of pure CO_2 on a realistic model of amine functionalized MCM-41 by simulation studies. Jing et al. [10] studied the adsorption of CO_2, N_2 and their mixtures on MCM-41 material, but did not investigate the effect of water vapor on the adsorption behavior. Pajzderska et al. [11] studied the behavior of water confined in the pores of MCM-41 material using ^1H NMR and molecular dynamics simulation. They observed that at low filling, water molecules remained close to the pore surface, whereas at higher fillings water molecules were present away from the surface as well; however, the dynamics of water molecules was much slower than in bulk water. Coasne et al. [12] used grand canonical Monte Carlo (GCMC) simulations to study the solubility of CO_2, N_2 and CH_4 in water confined in pores of ZSM-5, MCM-41 and MIL-100. They observed significant enhancement in the solubility of the gases in confined water over that in bulk water. Mason et al. [1] studied the adsorption of gaseous mixture of CO_2, N_2 and H_2O in several microporous and mesoporous adsorbents, including amine-grafted MCM-41, using high-throughput analyzer. In amine-grafted MCM-41 samples, although the presence of water was observed to affect the amount of CO_2 adsorbed, the exact behavior depended on the type of amine.

In the present work, we conducted a detailed adsorption study of CO_2, N_2, O_2, water vapor and their mixtures on three different realistic molecular models of MCM-41 using grand canonical Monte Carlo (GCMC) simulations. Adsorption of pure gases, and binary, ternary and quaternary mixtures were studied at different temperatures and mixture compositions to determine the effect of the presence of water vapor and oxygen in flue gas mixtures on CO_2 adsorption and CO_2/N_2 separation in mesoporous silica adsorbents.

MODEL AND SIMULATION DETAILS

Three different molecular models of MCM-41, referred to as model 1, model 2 and model 3, were investigated to study gas ad-

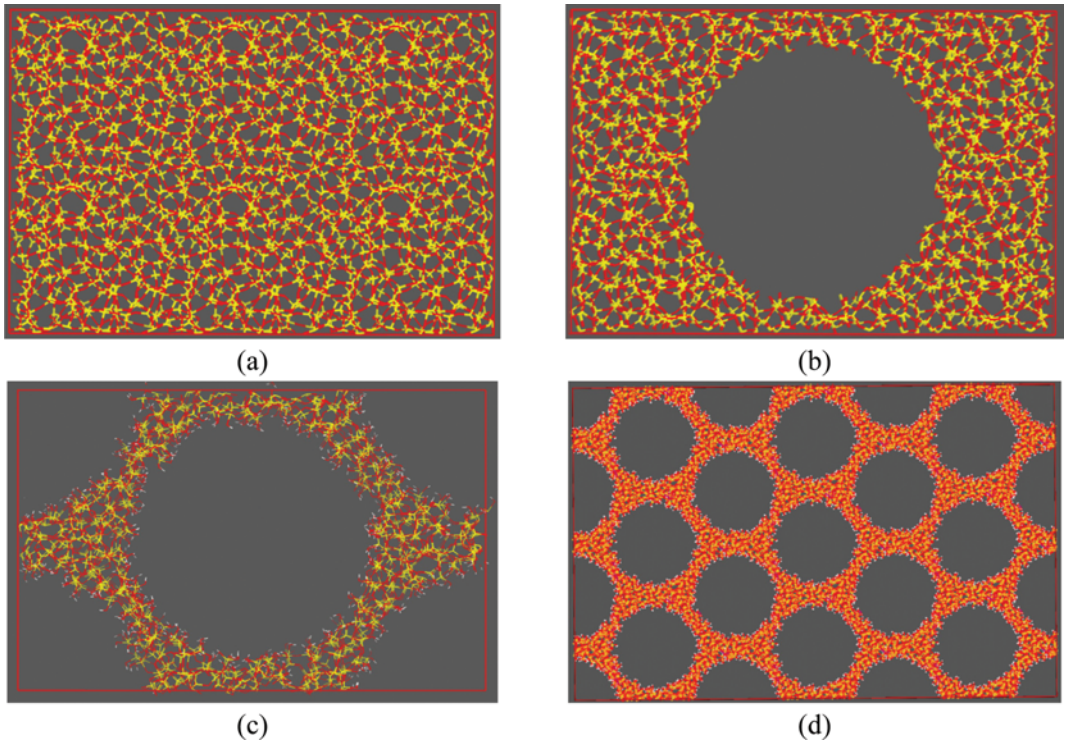

Fig. 1. (a) Amorphous block of silica matrix, (b) principal pore, (c) unit simulation box with surface hydroxyl groups attached, after geometry optimization, (d) periodic replication to obtain hexagonal array of pores.

sorption and separation. Model 1 was constructed by carving cylindrical pores (approximately 36 Å in diameter) in a block of amorphous silica matrix (taken from the database of structures available in the Materials Studio 7.0 software [13]) while maintaining the regular hexagonal arrangement of the pores, as shown in Fig. 1(d). Creation of pores resulted in unsaturated Si and O sites on the pore surface. To saturate these dangling bonds, a simple rule was followed that involved identifying the atoms having one or more dangling bond(s). Silicon atoms with exactly three dangling bonds were replaced with hydrogen atoms, whereas those having fewer than three dangling bonds were saturated with appropriate number of hydroxyl (-OH) groups (one or two). Similarly, dangling bonds of oxygen atoms were saturated with H atoms. Si-O and O-H bond lengths were taken to be 1.61 Å and 1.1 Å, respectively [17], for addition of H atoms and -OH groups. The geometry of the MCM-41 structure thus obtained was optimized. Fig. 1(a) shows the initial amorphous silica block, Fig. 1(b) shows the principal cylindrical pore, and Fig. 1(c) shows the simulation box containing the principal pore and four quarter pores, where the dangling bonds on the pore wall have been saturated and geometry has been optimized. Hexagonal arrangement of the cylindrical pores was obtained by application of periodic boundary condition in all three direction (x, y and z), as shown in Fig. 1(d) where the simulation box has been replicated three times in the x and y directions. Model 2 was derived from purely crystalline silica framework of cristobalite (structure taken from the crystallographic database [14]). The cristobalite unit cell was replicated 6×6×9 times in x, y and z direction to create a crystalline cuboidal block. Molecular dynamics (MD) simulations were carried out on the cristobalite block at high temperature using Materials Studio 7.0 software [13] to disrupt the crystalline structure and generate disorder in the regular arrangement. Cylindrical pores having a diameter of approximately 36 Å were then carved in the framework, dangling bonds were saturated and geometry was optimized. The methodology used for saturating the dangling bonds was identical to that employed during generation of model 1. Model 3 of MCM-41 was taken from Ugliengo et al. [15], which was developed by inducing disorder in a hexagonal supercell of α-quartz through classical molecular dynamics at high temperature, cutting the pore, appropriately saturating the dangling bonds with H atoms or -OH groups, and optimizing the obtained structure using density functional theory (DFT). Pore diameters in all the models considered here lie in the range typically observed in real MCM-41 adsorbents [16]. Unit simulation boxes of the three models used in this work are shown in Fig. 2.

For models 1 and 2, Forcite module of Materials Studio 7.0 software [13] was used to carry out geometry optimization employing the DREIDING force field [18], which includes both bonded and non-bonded interaction terms. Non-bonded interactions were computed as the sum of Lennard-Jones (LJ) potential and Coulombic interaction as given by Eq. (1).

$$u_{ij}(r) = 4\varepsilon_{ij}\left[\left(\frac{\sigma_{ij}}{r_{ij}}\right)^{12} - \left(\frac{\sigma_{ij}}{r_{ij}}\right)^{6}\right] + \frac{q_i q_j}{4\pi\varepsilon_0 r_{ij}} \quad (1)$$

where $u_{ij}(r)$, ε_{ij}, σ_{ij}, r_{ij}, q_i, q_j and ε_0 are the non-bonded potential energy, LJ well depth, LJ size, distance between the two sites i and j, charges on i^{th} and j^{th} site and permittivity of vacuum, respectively. The van der Waals interactions were computed using a cutoff distance of 12.5 Å, and the Coulombic interactions were calculated using the Ewald sum method [19]. Charges on individual atoms were estimated from the charge equilibration (QEq) method [20]. Geometry optimization was not carried out for model 3 because the structure taken from [15] was already optimized using DFT calculations.

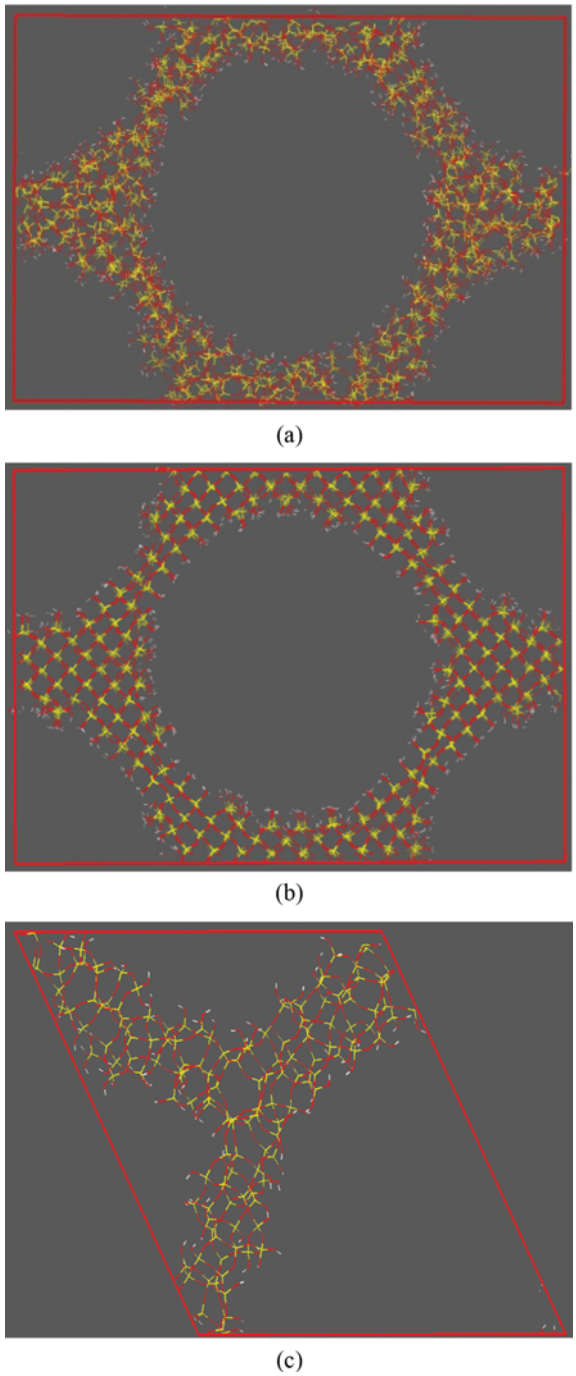

Fig. 2. Simulation box of (a) model 1, (b) model 2, (c) model 3.

The three MCM-41 models were characterized by determining the X-ray diffraction (XRD) pattern, surface area, accessible pore volume and radial distribution function (RDF). XRD pattern, Connolly surface area [21] and accessible pore volume for all the mod-

els were calculated using the Materials Studio 7.0 software. XRD patterns of MCM-41 models were simulated using Cu Kα (λ= 1.5406 Å) radiation. Diffraction data were recorded in the 2θ range of 1-8° with a step size of 0.05. Connolly surface area and accessible pore volume were calculated by rolling a spherical probe having a radius of 1.4 Å on the surface of the adsorbent pores. The accessible surface area was calculated using nitrogen probe of radius 1.82 Å. RDF is the probability distribution of finding particles/atoms of a certain type in a spherical region around another central particle/atom of same or different type. Thus, Si-Si RDF in the MCM-41 framework provides a measure of how Si atoms are spatially distributed with respect to each other, whereas Si-O RDF indicates how O atoms are distributed with respect to the Si atoms. The Si-Si, O-O, Si-O, O-H and H-H RDFs were calculated for all three MCM-41 models considered. In addition, the adsorbate-adsorbent (C_{CO2}-$O_{MCM\text{-}41}$) and adsorbate-adsorbate (C_{CO2}-C_{CO2}) RDFs were calculated to study the distribution of adsorbed CO_2 in the MCM- 41 pores.

GCMC [22] simulations were performed using the Towhee software package [23] to study the adsorption of CO_2, N_2, O_2, H_2O and their mixtures in the MCM-41 models. In this work, N_2 [24] and O_2 [25] were modeled as having two LJ interaction sites at the respective atom positions and three sites with partial charges (two sites at the two atom positions and one at the center of mass) to capture the effect of quadrupole moment of these small molecules. A three-site model was employed for CO_2, with the sites located at the respective atom positions and each site having an LJ interaction center and partial charge. The detailed force field parameters for the adsorbate gases as well as the adsorbent (MCM-41) were taken from literature and are summarized in Table 2.

The chemical potential values of the adsorbate gases, provided as input to the GCMC simulations, were calculated for each pure adsorbate species as well as mixture of adsorbate molecules by Monte Carlo (MC) simulations of the bulk gas (pure or mixture) in the isothermal-isobaric (constant NPT) ensemble using the Towhee software package at the appropriate temperature and pressure. For this purpose, a simulation box containing only the gas molecules (of one or more type depending on whether pure gas or mixture is being considered) was first equilibrated at the desired temperature and pressure (at which we sought to obtain the adsorption loading) by carrying out MC simulations in the constant NPT ensemble. After the density of the simulation box becomes relatively constant, the gas or gas mixture in the box is representative of the bulk gas phase at the temperature and pressure of interest. The chemical potential of the gas (or gases, if we are studying mixtures) was then calculated using the Towhee software by performing several trial insertions of gas molecules in the box and averaging the values of chemical potential obtained for each insertion. The force field employed for the gas molecules during equilibration and calculation of chemical potential is identical to that employed during the subsequent GCMC simulations.

The framework of MCM-41 was maintained rigid and frozen during the GCMC simulations, and thus, stretching, bending, torsion and inversion interactions were not considered within the framework. Stretching and bending interactions were considered only for water molecules and only stretching potential was considered for CO_2, N_2 and O_2 adsorbate molecules. GCMC simulation was carried out by applying four different types of GCMC moves [22]: insertion, deletion, translation and rotation. Insertion and deletion moves were assigned equal probability of 0.3 each, and rotation and translation were given equal probability of 0.2 each. In the case of mixture of two or more adsorbate species, particle swap moves (or identity exchange moves) [27] were performed in addition to the other four types of move to achieve faster equilibrium. Non-bonded interactions were computed as the sum of LJ potential and Coulombic interactions (see Eq. (1)). A cutoff of 12 Å was used for the LJ potential along with tail correction. Lorentz-Berthelot mixing rules (Eqs. (2) and (3)), were applied for calculation of LJ potential parameters between unlike species.

$$\sigma_{ij}=\frac{\sigma_{ii}+\sigma_{jj}}{2} \tag{2}$$

$$\varepsilon_{ij}=\sqrt{\varepsilon_{ii}\times\varepsilon_{jj}} \tag{3}$$

Electrostatic interactions were calculated by the Ewald summation technique [19]. Five million GCMC steps were run, and data from the last 2.5 million steps were used for calculating the average ad-

Table 2. LJ potential parameters, charges and bond lengths in adsorbent and adsorbate molecules

Molecule	Site	σ (Å)	ε (K)	q (e)	Bond length (Å)
MCM-41 [10]	Si	3.804	155.858	0.1222	
	O	3.033	48.115	−0.0615	
	H	2.846	0.050	0.0318	
CO_2 [10]	C	3.473	47.813	0.6040	1.152 (C=O)
	O	3.033	48.115	−0.3020	
N_2 [24]	N	3.310	36.000	−0.4820	1.10 (N≡N)
	N(COM)†	0.000	0.000	0.9640	
O_2 [25]	O	3.020	49.000	−0.1130	1.210 (O=O)
	O(COM)†	0.000	0.000	0.2260	
H_2O [26]*	H	0.000	0.000	0.4238	1.0 (O-H)
	O	3.166	78.197	−0.8476	

†COM stands for center of mass

*H-O-H angle (water model SPCE [26])=109.47°

Table 3. Structural characteristics of the MCM-41 models

Properties	Model 1	Model 2	Model 3	MCM-41 (Experimental)
Simulation box dimensions (Å)	42.8, 42.8, 64.2	42.96, 42.96, 64.44	40.60, 40.60, 36.60	
Simulation box angles (°)	90, 90, 90	90, 90, 90	90, 90, 120	
Specific surface area (m^2/g)	1225.71	1260.51	1386.36	1090-1150 (from [28,29])
Accessible pore volume (cm^3/g)	0.547	0.490	0.499	
Skeletal density (g/cm^3)	2.48	2.345	2.26	2.2 (from [2])
OH group density ($/nm^2$)	4.79	4.45	4.68	

sorbed amounts for adsorption simulation of pure gases and mixtures not containing water. Adsorption simulations of mixtures containing water vapor as one of the components were carried out for eight million steps; again, data from the last four million steps were used for averaging. GCMC simulations provide the absolute amounts adsorbed in the simulation box, which were converted to excess adsorbed amounts for direct comparison to experimental isotherms. Excess number density in the adsorbed phase was computed by subtracting the bulk number density from the absolute number density obtained from simulation, as given in using Eq. (4)

$$N_{ex\text{-}ad} = N_{sim} - V_b \times \rho_{cal} \quad (4)$$

where $N_{ex\text{-}ad}$ is the excess adsorbed amount, N_{sim} is the absolute number of adsorbed molecules obtained from GCMC simulation, V_b is the solvent (helium) accessible pore volume in the simulation box, and ρ_{cal} is the bulk number density of the adsorbate in the gas phase. ρ_{cal} is obtained by carrying out constant NPT MC simulations on only the adsorbate species at the same temperature and pressure as that of the respective GCMC simulation. After constant NPT MC equilibration of the adsorbate species in the bulk gas phase at constant temperature and pressure, the system attains the appropriate density, which is used as ρ_{cal} in Eq. (4).

For binary, ternary and quaternary mixtures, the appropriate molar ratio of the different components in the gas mixture was ensured by providing the corresponding chemical potential value of the component as input to the GCMC simulation. MC simulation of the bulk gas mixture was first carried out in the constant NPT ensemble, where the molar content of the different species in the gas mixture was maintained by ensuring correct ratio of the number of molecules of each species in the simulation box. For example, to simulate an equimolar (50 : 50) binary mixture of 200 molecules in the simulation box, the number of molecules of each species was maintained at 100. After equilibration, chemical potentials for each species in the gas mixture were calculated using the Towhee software package. These chemical potential values, which correspond to the temperature, pressure and molar composition of the simulated bulk gas phase, were then used in the GCMC simulations for adsorption in the MCM-41 models.

RESULTS AND DISCUSSION

1. Characterization of MCM-41 Models

The structural characteristics of the MCM-41 models were determined by calculating the specific surface area, pore volume, skeletal density and surface hydroxyl group density. To compare the experimental BET surface area of MCM-41 with the corresponding surface area of the MCM-41 models, a spherical probe of diameter 3.64 Å (representative of nitrogen molecule) was rolled over the surface of the pores of the models. The surface area thus obtained compared favorably with the reported experimental values of BET surface area of MCM-41 in the range 1,090-1,150 m^2/g [28,29]. The slight discrepancy between the calculated accessible surface areas and the experimental surface areas could possibly be due to the fact that actual MCM-41 material shows a distribution of pore sizes, whereas in the models we have considered a single pore size, at a value representative of the average pore size of real MCM-41 materials. Further, the exact roughness and atomic arrangement of MCM-41 pore surface is not known experimentally, and the models just attempt to capture the pore wall roughness to a reasonable accuracy. Nevertheless, all models show reasonably good agreement with experimental data, with the agreement being best for Model 1. Table 3 lists the various structural characteristics of the three MCM-41 models.

Powder XRD patterns for all the three models were simulated using Materials Studio 7.0 [13], and are shown in Fig. 3 along with an experimental XRD pattern for real MCM-41 sample (adapted from [16]). The location of the first low-angle XRD peak of the MCM-41 models, indicating the (100) plane, matches well with that of the experimental XRD pattern; however, the experimental XRD peak is much broader due to the more amorphous nature of

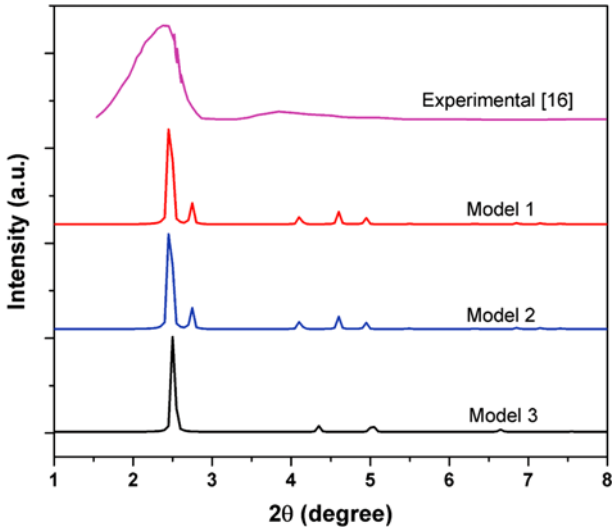

Fig. 3. Powder XRD diffraction pattern of the three models compared with experiment (data from Loganathan et al. [16]).

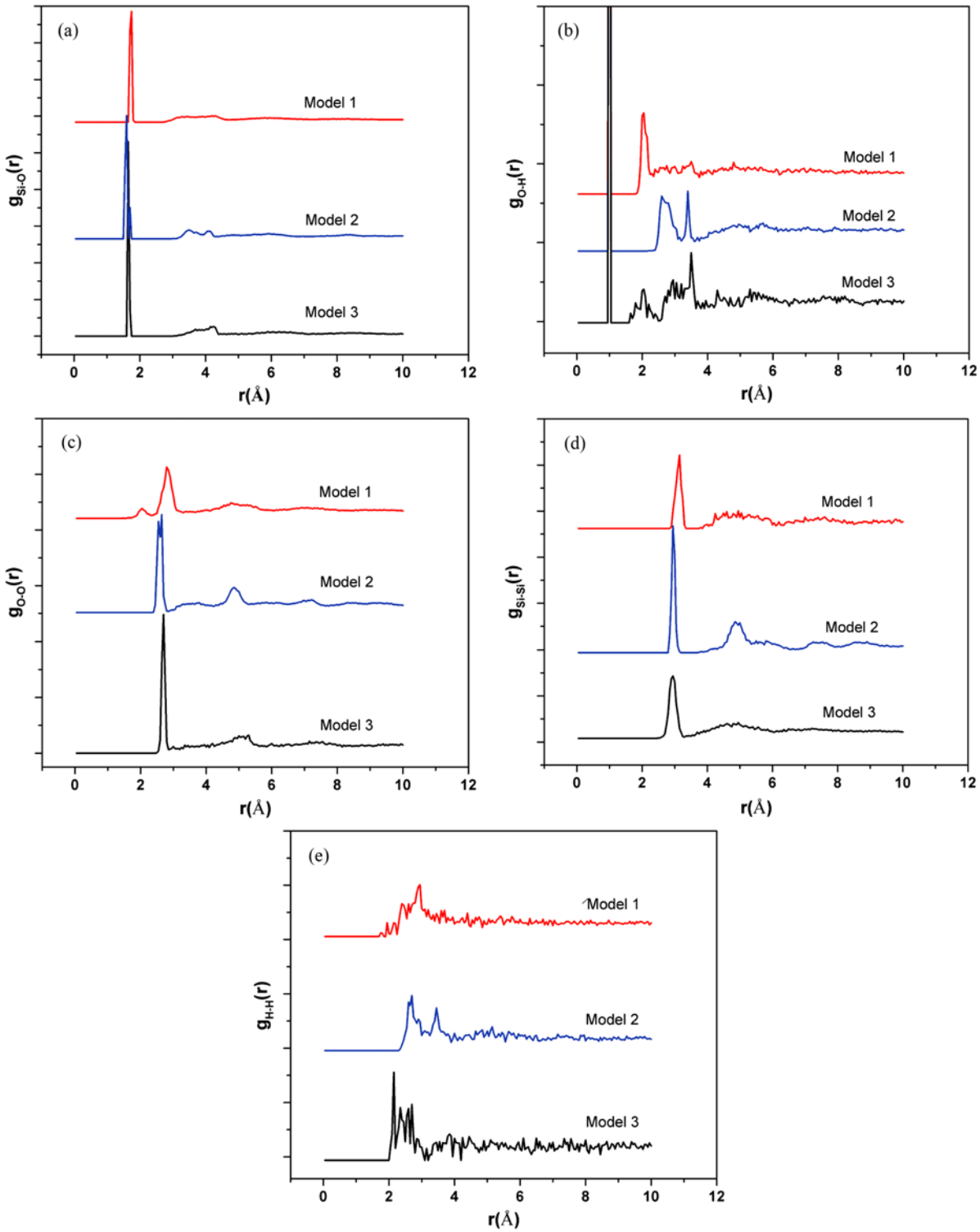

Fig. 4. Radial distribution functions of the three models for the atomic pairs (a) Si-O (b) O-H (c) O-O (d) Si-Si and (e) H-H. The RDFs for the models have been shifted vertically for ease of visualization. In (b), all three models show strong peaks at ~1 Å, and the peak of model 3 almost completely overlaps with the peaks of the other models.

the actual material. Fig. 4(a) to 4(e) show plots of the RDFs for Si-O, O-H, O-O, Si-Si and H-H in the three models. RDF is a measure of the probability of finding atoms of a certain type in the neighborhood of a central atom (of same or different type). Thus, the sharp first peaks in the Si-O (Fig. 4(a)) and O-H (Fig. 4(b)) RDFs indicate a very narrow distribution of the Si-O and O-H bond lengths in the three MCM-41 models. The Si-O bond lengths in the models are in good agreement with the Si-O bond lengths

observed in quartz and α-cristobalite [30]. The absence of any small peaks before the first prominent sharp peak also confirms that no strained bonds or significant structural overlaps are present. Fig. 4(b) also indicates the possible presence of hydrogen bonding in 3 (and to some extent, in model 1), where a second broad peak is observed at r~2 Å. The first peaks in Fig. 4(c) and 4(d) correspond to the O-O and Si-Si distances of the O-Si-O and Si-O-Si linkages, respectively, in the model frameworks. These next-bonded-neighbor peaks are in general broader than the bonded-neighbor peaks shown in Fig. 4(a) and 4(b), due to the disordered nature of the MCM-41 wall. Peaks for model 1 are broader than the corresponding peaks for the other two models, which suggests that model 1 is more disordered. The hydrogen atoms present in the hydroxyl groups on the pore surface are well-separated and do not show any significant overlap, as is evident from Fig. 4(e) which shows that no other hydrogen atoms are present within 2 Å of a given hydrogen atom.

2. Adsorption of Pure Gases

Adsorption of pure CO_2 on all three models was studied by GCMC simulation and the results were compared with the experimental results of Seaton et al. [2] at two different temperatures: 273.2 K and 303.2 K. At both temperatures the simulated adsorption isotherm for model 1 was found to be in good agreement with the experimental results over the entire pressure range considered, as shown in the Fig. 5(a) and (b). CO_2 isotherms for model 3 also show reasonable agreement with experimental results for low to moderate pressures but deviate at high pressures. However, model 2 underpredicts the amount of CO_2 adsorbed over the entire pressure range.

The isosteric heats of adsorption, ΔH^{st}_{ads}, of CO_2 on the different models were calculated as [31,32]

$$\Delta^{st}_{ads} = \frac{\langle UN\rangle_\mu - \langle U\rangle_\mu \langle N\rangle_\mu}{\langle N^2\rangle_\mu - \langle N\rangle_\mu \langle N\rangle_\mu} - \langle U_g\rangle - k_B T \quad (5)$$

where $\langle \ldots \rangle_\mu$ represents average value in the grand canonical ensemble. U, N and T represent system energy, number of particles (adsorbate molecules) and temperature, respectively, $\langle U_g \rangle$ represents the average energy of a single isolated adsorbate molecule (in the absence of the adsorbent) and k_B is the Boltzmann constant. Fig. 6 shows the isosteric heats of adsorption of CO_2 on the three models and experimental data from He and Seaton [3]. The values for model 1 show good match with experiment over the entire loading range, whereas the values for models 2 and 3 compare less favorably. Model 1 also shows a decreasing trend in ΔH^{st}_{ads} values with increasing loading, consistent with experimental results. The decrease in the number of available sites for adsorption unfavorably affects the adsorbent-adsorbate interactions, leading to decrease in ΔH^{st}_{ads} values. Model 2 slightly underpredicts the isosteric heat values while model 3 overpredicts the values.

RDF was also calculated for adsorbate carbon atoms with respect to the adsorbent oxygen atoms (C-O_{ads}) and the carbon atom cen-

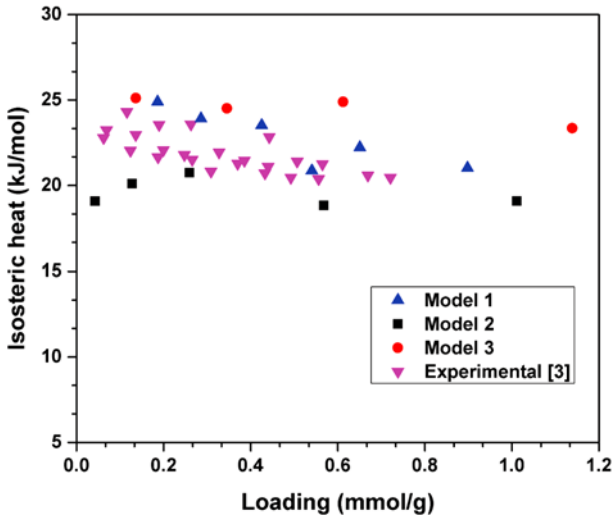

Fig. 6. Isosteric heats of adsorption of CO_2 in the three MCM-41 models compared with experimental values (from He and Seaton [3]) at 298 K.

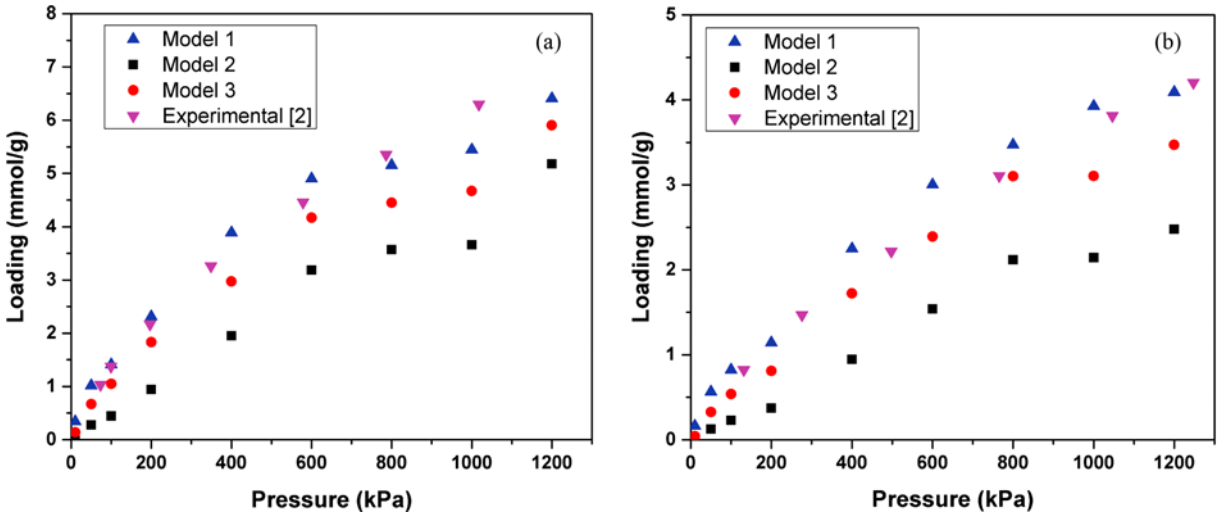

Fig. 5. (a) Pure CO_2 adsorption isotherm at 273.2 K for the three models compared to experiment (experimental data from He and Seaton [2]). (b) Pure CO_2 adsorption isotherm at 303.2 K for the three models compared to experiment (experimental data from He and Seaton [2]).

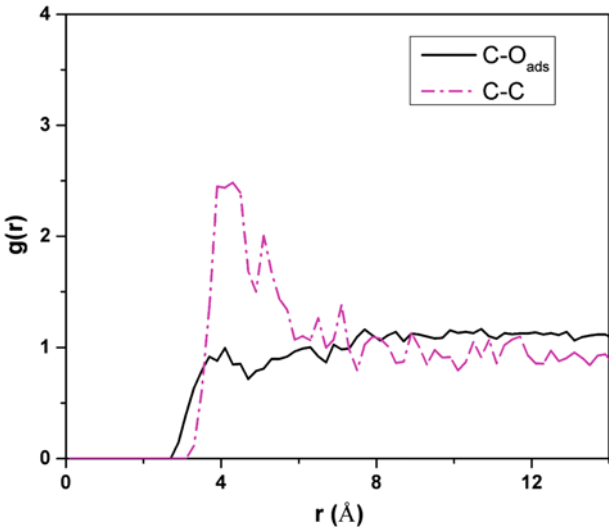

Fig. 7. Adsorbate(C)-adsorbent(O) and adsorbate(C)-adsorbate(C) RDFs at 10 bar and 303.2 K for CO_2 adsorption in model 1.

ters of other adsorbate molecules (C-C) to investigate the spatial arrangement of the CO_2 molecules inside the pore. The RDFs shown in Fig. 7 for CO_2 adsorption in model 1 suggest that even at high loading CO_2 molecules do not show any preferential arrangement about the oxygen atoms of the framework. The RDF of CO_2 molecules around oxygen atoms was calculated by averaging over all the oxygen atoms in the MCM-41 framework. RDF of CO_2 molecules may show some peak if only the oxygen atoms on the pore surface are considered; however, CO_2 will definitely not show any preferential arrangement with respect to the oxygen atoms located deep in the pore walls of the framework (away from the surface). Therefore, the average RDF of CO_2 considering all oxygen atoms in the framework also does not show any noticeable peaks. Note from Table 2 that the value of the LJ well depth (ε) of silicon atoms is much higher than that of the framework oxygen atoms. Hence, the framework silicon atoms are expected to have much stronger van der Waals interactions with the adsorbate gases than the framework oxygen atoms. Fig. 7 also shows the C-C RDF for the adsorbed CO_2 molecules. The first peak position of this RDF suggests that the carbon centers of the nearest CO_2 molecules are separated by ~4 Å.

3. Binary, Ternary and Quaternary Gaseous Mixture Adsorption

Binary mixture adsorption simulations were performed on models 1 and 3, which showed acceptable agreement with the pure CO_2 experimental adsorption data (see previous section), whereas model 2 was not considered further. Binary CO_2/N_2 gas mixtures were studied at two different molar compositions, namely 0.5 : 0.5 and 0.15 : 0.85 (CO_2 : N_2). Fig. 8(a)-(c) show the plots of binary gas adsorption isotherms on the two models at the two compositions. Due to its larger quadrupole moment and stronger van der Waals interactions, CO_2 interacts more favorably with the MCM-41 framework than N_2 resulting in higher loading of CO_2 at both bulk gas compositions. Even at flue gas composition (with 85% N_2), amount of CO_2 adsorbed was found to be higher than that of N_2 in both the models (Fig. 8(a) and 8(b)). Fig. 8(c) shows that the adsorp-

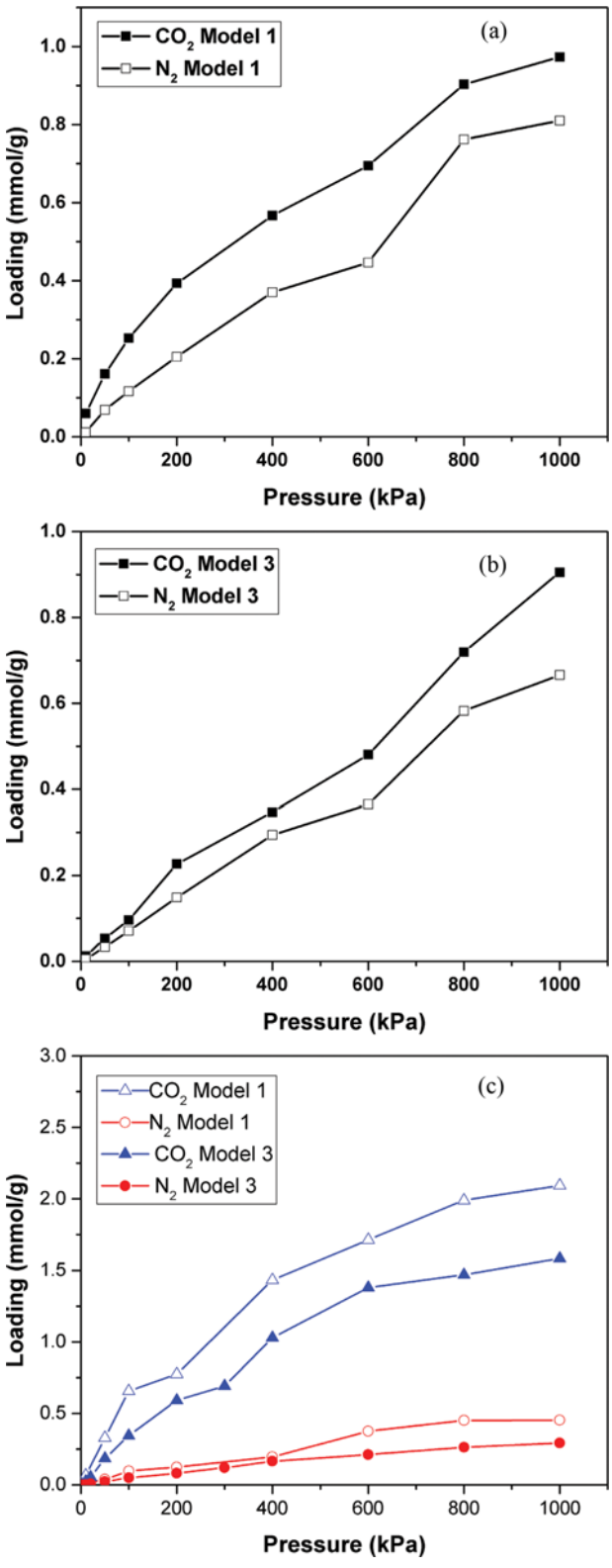

Fig. 8. (a) Adsorption isotherms for binary CO_2/N_2 mixture of composition 15 : 85 in model 1 at 303.15 K (lines are drawn only to guide the eye). (b) Adsorption isotherms for binary CO_2/N_2 mixture of composition 15 : 85 in model 3 at 303.15 K (lines are drawn only to guide the eye). (c) Adsorption isotherms for adsorption of equimolar binary CO_2/N_2 mixture in models 1 and 3 at 303.15 K (lines are drawn only to guide the eye).

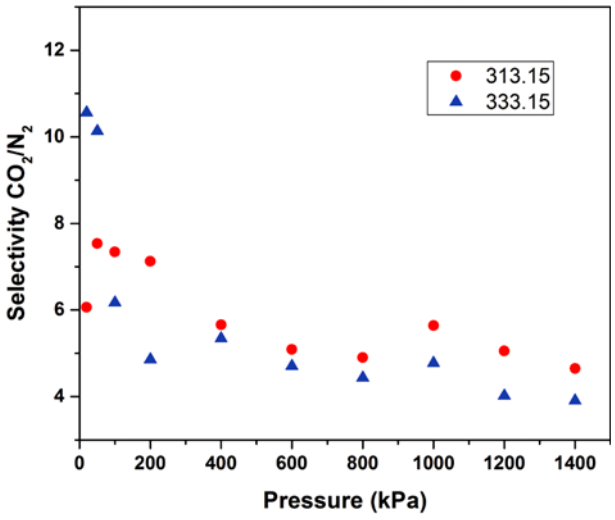

Fig. 9. Selectivity of CO_2 over N_2 for adsorption of equimolar binary CO_2/N_2 mixture on model 1 of MCM-41 at two different temperatures (in K).

tion loadings of both CO_2 and N_2 are higher in model 1 than in model 3. Selectivity of CO_2 over N_2 (S_{CO_2/N_2}) is defined as

$$S_{CO_2/N_2} = \frac{X_{CO_2}/X_{N_2}}{Y_{CO_2}/Y_{N_2}} \quad (6)$$

where X_{CO_2} and X_{N_2} are the respective mole fractions of CO_2 and N_2 in the adsorbed phase, and Y_{CO_2} and Y_{N_2} are the respective mole fractions of CO_2 and N_2 in the bulk gas phase. Selectivities of CO_2 over N_2 for adsorption of equimolar bulk gas mixture in model 1 at two different temperatures are shown in Fig. 9. The selectivities at both the temperatures lie primarily in the range of 4-8, and show a general decreasing trend with increasing pressure, although the reduction is not very pronounced. Further, the selectivities show a decreasing trend with temperature in general, which is consistent with the fact that the factor primarily responsible for higher selectivity of CO_2 over N_2 (i.e., their relative strengths of interaction with MCM-41) becomes less dominant as the temperature (and hence the kinetic energy) is increased. The observed CO_2/N_2 selectivity is comparable to values reported in literature for other unfunctionalized porous materials such as nanoporous carbon [33] and ordered mesoporous carbon [34]. Zhou et al. [33] reported CO_2/N_2 selectivity of ~4 at 298 K, 100 kPa for unfunctionalized nanoporous carbon having a surface area of 3,191.09 m^2/g using GCMC simulations whereas Yuan et al. [34] reported CO_2/N_2 selectivity of ~8 at 318 K, 100 kPa for synthesized ordered mesoporous carbon having a surface area of 2,255 m^2/g. In comparison, the CO_2/N_2 selectivity of MCM-41 model 1 is ~7-8 at 100 kPa, 313 K (see Fig. 9). Microporous metal-organic frameworks such as CuBTC have been reported to exhibit somewhat higher CO_2/N_2 selectivity (~20 at 298 K and 100 kPa for CuBTC [35]).

Fig. 10(a) and (b) show the distribution of the adsorbate molecules inside the pore of MCM-41 (model 1) at different pressures. To calculate the distribution, the pore was divided into concentric annular cylindrical bins of thickness 0.5 Å centered at the pore axis, and for each bin the number of adsorbate molecules whose center of mass was inside the bin was counted. The resulting number of adsorbate molecules in each bin was plotted against the radial distance of the bin from the center of the pore. As expected, the number densities of both the adsorbates show peaks close to the pore wall at both pressures. As CO_2 interacts more strongly with the pore wall, its peak intensity is significantly higher than that of N_2. Further, as the pressure is increased from 1 to 10 bar, the amount adsorbed increases significantly resulting in higher peaks for both the adsorbates at the higher pressure. Fig. 10(a) shows that at 1 bar pressure, adsorption primarily takes place very close to the pore wall (within a distance of ~5-6 Å from the pore wall). In contrast, at a higher pressure of 10 bar, the distribution is broader for both the adsorbates with an elongated tail that extends up to ~9 Å from the pore wall. The favorable adsorption sites on the pore wall are almost completely occupied, and onset of multilayer adsorption is observed. Fig. 11(a)-(d) show snapshots of binary CO_2-N_2 equimolar adsorption in model 1 over the pressure range of 0.5-12 bar. At 0.5 bar, the pore wall is mostly uncovered and adsorption of CO_2 is strongly preferred over N_2. As the pressure is increased, the wall coverage progressively increases; at 12 bar, almost the entire pore

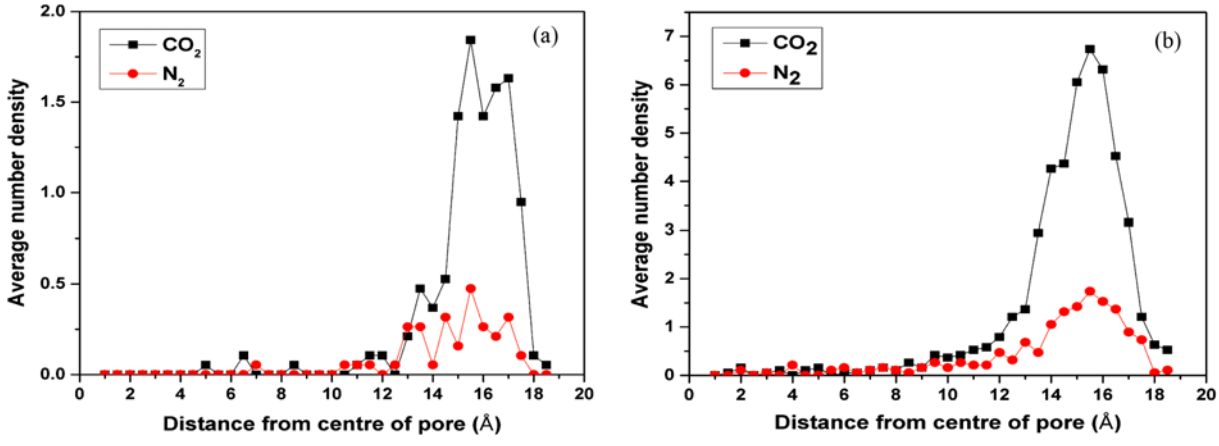

Fig. 10. Number density of adsorbate molecules in the principal pore of model 1 of MCM-41 for adsorption of equimolar binary CO_2/N_2 mixture at (a) 1.0 bar, and (b) 10 bar at 303.15 K.

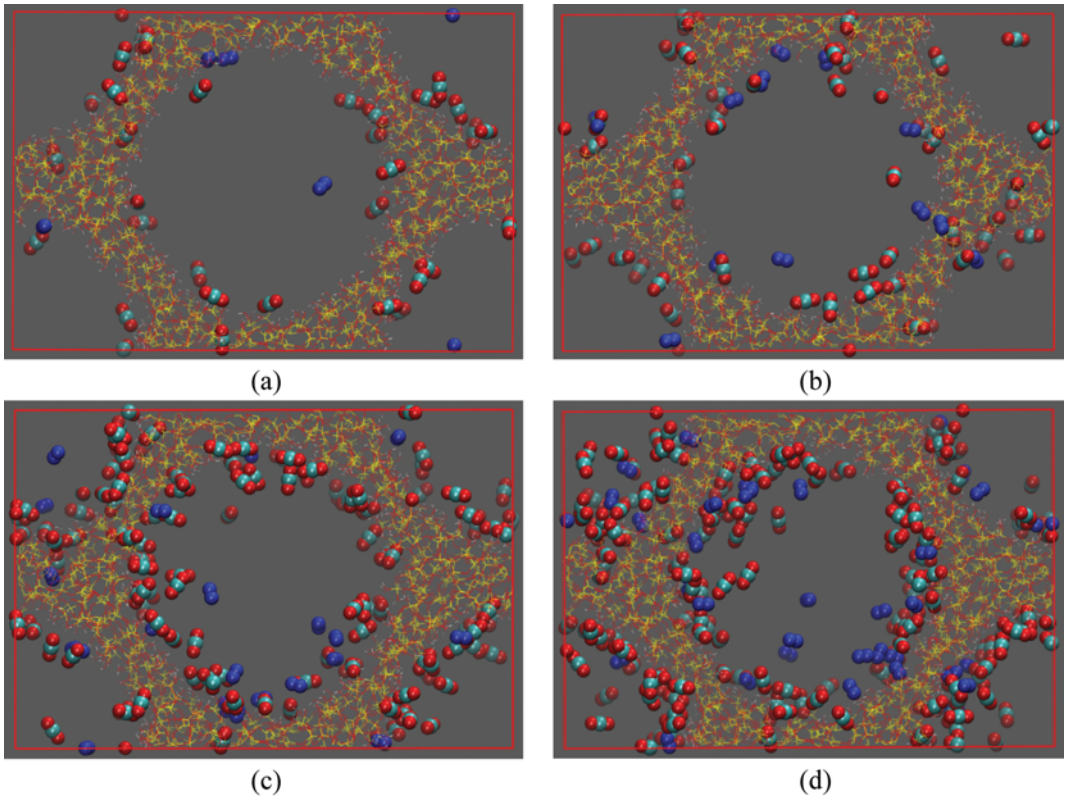

Fig. 11. Snapshots of adsorbed CO_2 and N_2 molecules in model 1 of MCM-41 for adsorption of equimolar mixture at (a) 0.5 (b) 2.0 (c) 6.0 and (d) 12.0 bar at 303.15 K.

surface is covered and evidence of adsorption in a second layer can be seen (Fig. 11(d)).

The ternary and quaternary mixture adsorption were carried out only for model 1 as this model showed the best agreement with experimental data for pure CO_2 adsorption. Presence of unburnt oxygen gas in the flue gas [36] was investigated at a $CO_2:N_2:O_2$ composition of 15 : 80 : 5. Adsorption and separation was studied at two different temperatures: 303.15 and 323.15 K. Partial charges were assigned to the O_2 molecule to account for the small quadrupole moment of O_2 (see Table 2). Fig. 12(a) and (b) show the adsorption isotherms of ternary mixture of $CO_2/N_2/O_2$ at two different temperatures. Comparison of Fig. 12(a) with the binary CO_2/

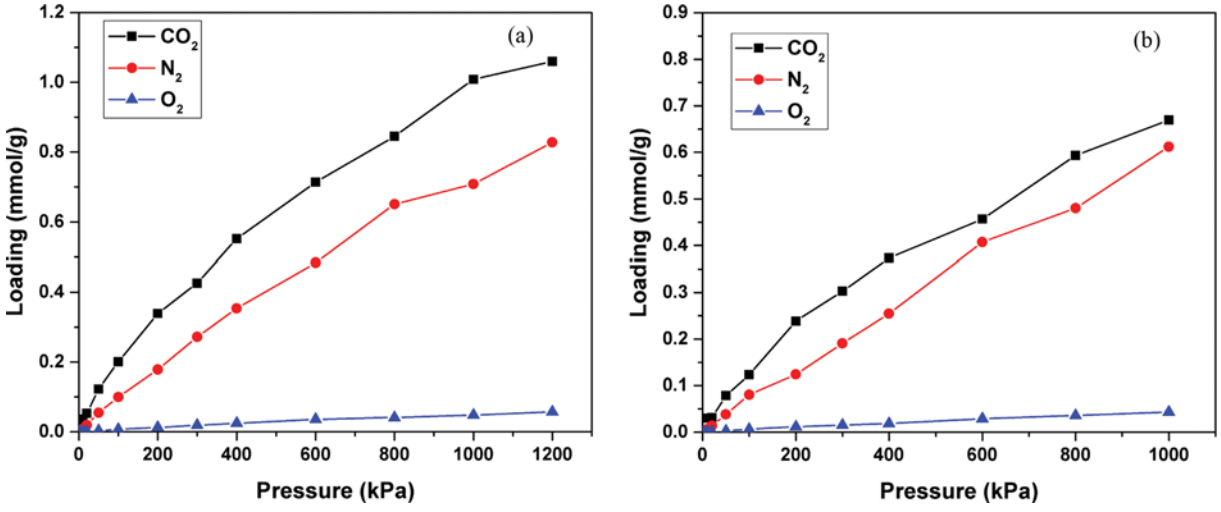

Fig. 12. (a) Adsorption isotherms of CO_2, N_2 and O_2 for ternary mixture adsorption of composition 15 : 80 : 5 ($CO_2:N_2:O_2$) in model 1 of MCM-41 at 303.15 K (lines are drawn only to guide the eye). (b) Adsorption isotherms of CO_2, N_2 and O_2 for ternary mixture adsorption of composition 15 : 80 : 5 ($CO_2:N_2:O_2$) in model 1 of MCM-41 at 323.15 K (lines are drawn only to guide the eye).

N_2 adsorption isotherm in Fig. 8(a) shows that the presence of O_2 does not have any significant effect on adsorption capacity of CO_2. The size of O_2 molecules and their interactions with the adsorbent (MCM-41) are quite similar to those of N_2 molecules due to which the presence of O_2 in the ternary mixture does not significantly change the CO_2 loading from that of CO_2/N_2 binary mixture.

As water vapor is invariably present in flue gas, we studied the effect of water vapor on the adsorption and separation of CO_2/N_2 mixture. Adsorption simulations were carried out at two different temperatures (303.15 and 348.15 K) and at two different mole fractions of water vapor (5% and 10%) in the ternary $CO_2/N_2/H_2O$ mixture. As water is more polar than the other two adsorbates, it is expected to interact more strongly with the surface hydroxyl groups on the pore walls of MCM-41. Fig. 13 shows the adsorption isotherms of $CO_2/N_2/H_2O$ mixtures at the two different temperatures: 303.15 K and 348.15 K. In all the adsorption simulations of mixtures containing water vapor, the partial pressure of water vapor in the gas mixture was kept below its saturation pressure at the corresponding temperature. Adsorption simulations were conducted for two different compositions—one with low water vapor content (5 mol%) and the other with higher fraction of water vapor (10 mol%)—to explore the effect of water vapor content on CO_2 loading and CO_2/N_2 selectivity. It is evident from Fig. 13(a)-(d) that the amount of water vapor adsorbed on MCM-41 in the pressure range studied is not significant. Although the polar water molecules are expected to interact strongly with the surface silanol groups of MCM-41, it appears that the surface density of silanol groups is not large enough to effect any significant adsorption of water at the low water vapor content in the gas phase and in the presence of other adsorbates, especially CO_2, which will compete for the adsorption sites. Further, a comparison of the low-pressure region of Fig. 8(a) with Fig. 13(a) shows that the presence of water vapor in the gas mixture does not have a substantial effect on the amount of CO_2 adsorbed as well as on CO_2/N_2 selectivity. Thus, CO_2/N_2 mixture adsorption behavior in MCM-41 is not significantly affected in the presence of up to 10 mol% water vapor in the gas mixture over a temperature range of 303.15-348.15 K (30 °C to 75 °C).

Flue gas may contain O_2 in addition to CO_2, N_2, and H_2O. Therefore, the adsorption of a quaternary mixture of CO_2, N_2, O_2 and H_2O was considered at a composition consistent with those observed in post-combustion carbon capture [37]. Adsorption of a

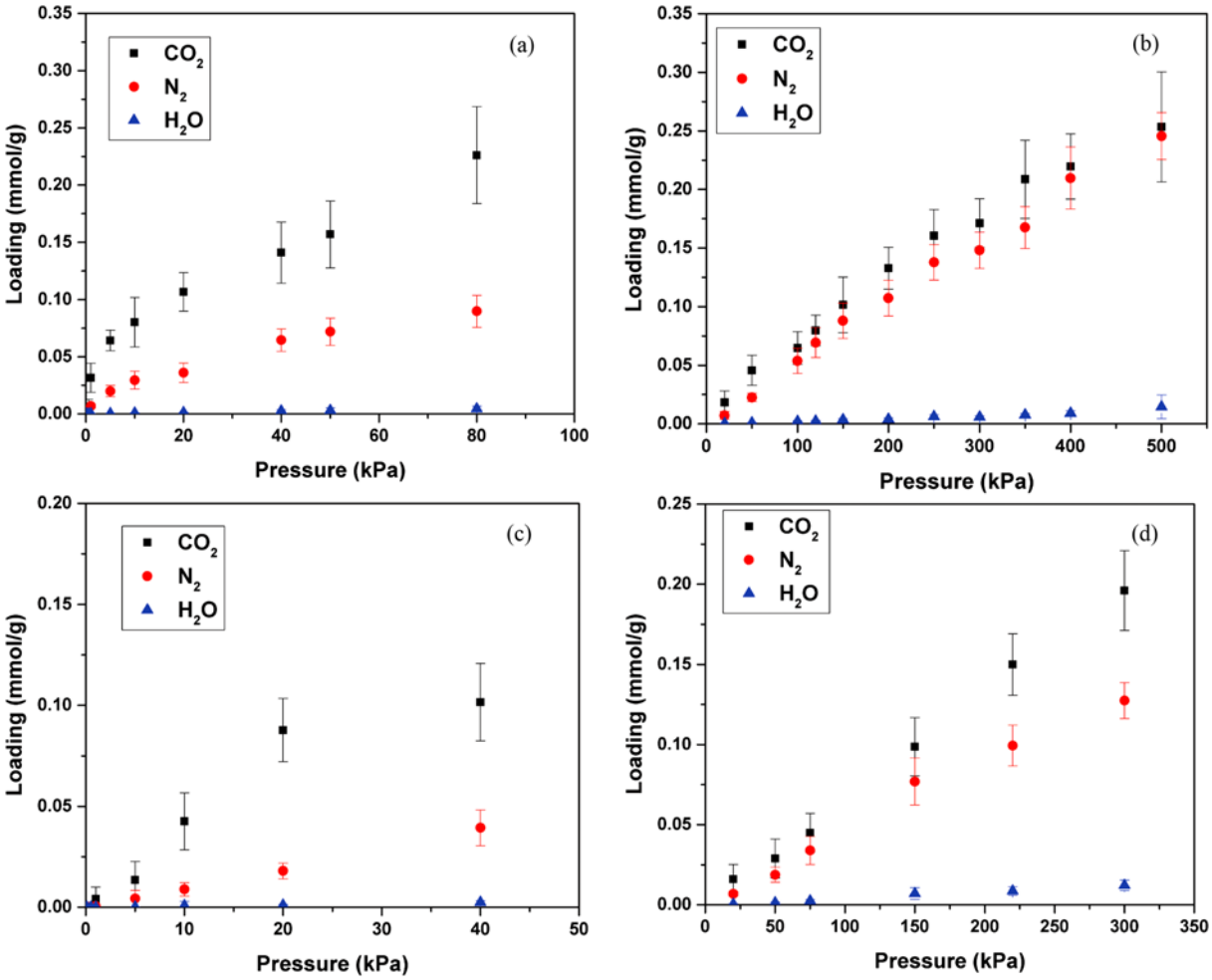

Fig. 13. Adsorption isotherms of CO_2, N_2 and H_2O for ternary mixture adsorption of composition 15 : 80 : 5 (CO_2 : N_2 : H_2O) at (a) 303.15 K, (b) 348.15 K, and for composition 15 : 75 : 10 (CO_2 : N_2 : H_2O) at (c) 303.15 K, (d) 348.15 K in model 1 of MCM-41.

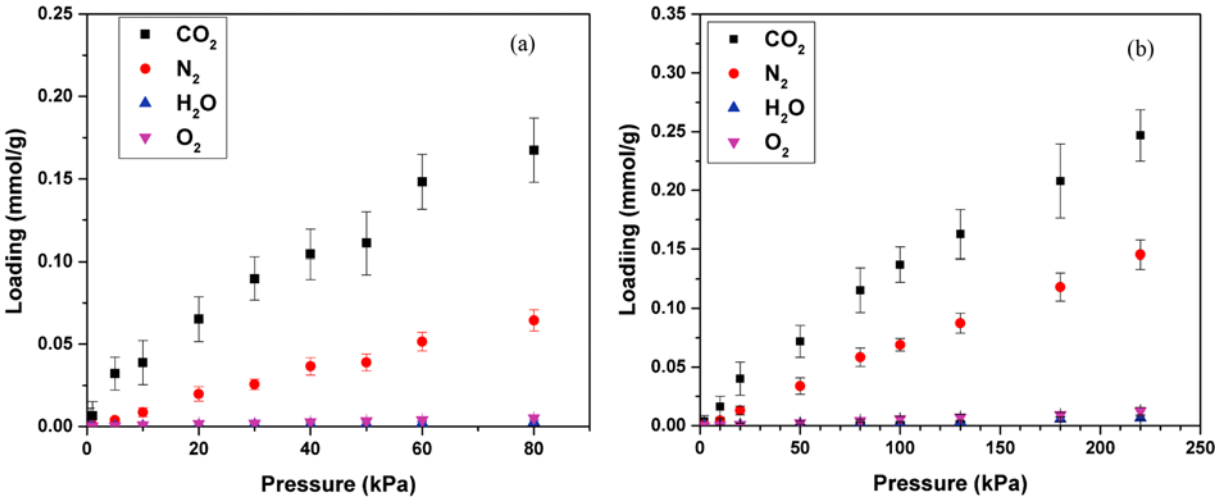

Fig. 14. Adsorption isotherms of CO_2, N_2, O_2 and H_2O for quaternary mixture adsorption of composition 15 : 75 : 5 : 5 (CO_2 : N_2 : O_2 : H_2O) at (a) 303.15 K, (b) 323.15 K in model 1 of MCM-41.

quaternary mixture of CO_2, N_2, O_2 and H_2O in the proportion 15 : 75 : 5 : 5 (by mole), respectively, was studied at two temperatures (303.15 K and 323.15 K). Adsorption isotherms at the two temperatures, shown in Fig. 14(a) and (b), reveal that the presence of O_2 and H_2O did not significantly affect the adsorption behavior of CO_2 and N_2. Further, the amount of H_2O adsorbed is slightly less than that of O_2 adsorbed (for identical gas-phase mole fractions), indicating the overall hydrophobic nature of MCM-41 pores. The surface density of silanol groups on MCM-41 pore walls is not high enough to cause significant adsorption of water.

CONCLUSIONS

We compared realistic molecular models of MCM-41 to study the adsorption of multicomponent gas mixtures representative of flue gas, and separation of CO_2 from such mixtures. The MCM-41 models were characterized by calculating the XRD pattern, RDF and surface area, and validated by comparing the results obtained with those reported for real MCM-41 samples. The pure CO_2 adsorption results predicted by model 1, prepared from a block of amorphous silica matrix with Si : O ratio of 1 : 2, were in better agreement with experimental results than those predicted by the other models. The adsorption of binary mixtures of CO_2 and N_2, ternary mixtures of CO_2, N_2 and H_2O and CO_2, N_2 and O_2, and quaternary mixture of CO_2, N_2, O_2 and H_2O was studied at different temperatures on MCM-41 model 1. Adsorption study of binary mixture of CO_2 and N_2 shows that CO_2 is preferentially adsorbed over N_2 at all the temperatures considered, owing to the stronger dispersion interactions and larger quadrupole moment of CO_2. The presence of small amounts of O_2 in the CO_2/N_2 mixture, whose size and interactions with MCM-41 are similar to N_2, does not affect the CO_2/N_2 selectivity. Further, ternary mixture simulations of CO_2/N_2/water vapor mixtures established that up to 10 mol% of water vapor in the gas mixture does not have a significant effect on CO_2 adsorption and CO_2/N_2 separation over a temperature range of 30-75 °C. Finally, adsorption studies of quaternary mixtures of $CO_2/N_2/O_2$/water vapor on MCM-41 did not reveal any significant effect of the simultaneous presence of O_2 and H_2O on the CO_2/N_2 adsorption behavior. Despite the presence of surface silanol groups on the pore walls, MCM-41 did not show any clear preference for the adsorption of the polar water molecules over O_2 (or N_2) molecules.

ACKNOWLEDGEMENTS

The authors wish to acknowledge the Department of Science and Technology, Government of India for FIST program support under project SR/FST/ET11-047/2010, which provided funding for the high-performance computing cluster used to carry out the simulations reported in this work.

REFERENCES

1. J. A. Mason, T. M. McDonald, T. H. Bae, J. E. Bachman, K. Sumida, J. J. Dutton, S. S. Kaye and J. R. Long, *J. Am. Chem. Soc.*, **137**, 4787 (2015).
2. Y. F. He and N. A. Seaton, *Langmuir*, **19**, 10132 (2003).
3. Y. F. He and N. A. Seaton, *Langmuir*, **22**, 1150 (2006).
4. C. T. Kresge, M. E. Leonowicz, W. J. Roth, J. C. Vartuli and J. S. Beck, *Nature*, **359**, 710 (1992).
5. Z. H. Luan, C. F. Cheng, W. Z. Zhou and J. Klinowski, *J. Phys. Chem.*, **99**, 1018 (1995).
6. P. B. Amama, S. Lim, D. Ciuparu, Y. H. Yang, L. Pfefferle and G. L. Haller, *J. Phys. Chem. B*, **109**, 2645 (2005).
7. J. H. Yun, T. Duren, F. J. Keil and N. A. Seaton, *Langmuir*, **18**, 2693 (2002).
8. S. Zhuo, Y. Huang, J. Hu, H. Liu, Y. Hu and J. Jiang, *J. Phys. Chem. C*, **112**, 11295 (2008).
9. S. Builes and L. F. Vega, *J. Phys. Chem. C*, **116**, 3017 (2012).
10. Y. Jing, L. Wei, Y. Wang and Y. Yu, *Chem. Eng. J.*, **220**, 264 (2013).
11. A. Pajzderska, M. A. Gonzalez, J. Mielcarek and J. Wasicki, *J. Phys. Chem. C*, **118**, 23701 (2014).

12. H. Linh Ngoc, Y. Schuurman, D. Farrusseng and B. Coasne, *J. Phys. Chem. C*, **119**, 21547 (2015).
13. Materials studio, Accerlys Inc., San Diego, U.S.A.
14. R. T. Downs and D. C. Palmer, *Am. Mineral.*, **79**, 9 (1994).
15. P. Ugliengo, M. Sodupe, F. Musso, I. J. Bush, R. Orlando and R. Dovesi, *Adv. Mater.*, **20**, 4579 (2008).
16. S. Loganathan, M. Tikmani and A. K. Ghoshal, *Langmuir*, **29**, 3491 (2013).
17. F. Tielens, C. Gervais, J. F. Lambert, F. Mauri and D. Costa, *Chem. Mater.*, **20**, 3336 (2008).
18. S. L. Mayo, B. D. Olafson and W. A. Goddard, *J. Phys. Chem.*, **94**, 8897 (1990).
19. B. A. Wells and A. L. Chaffee, *J. Chem. Theory Comput.*, **11**, 3684 (2015).
20. A. K. Rappé and W. A. Goddard III, *J. Phys. Chem.*, **95**, 3358 (1991).
21. M. L. Connolly, *J. Appl. Crystallogr.*, **16**, 548 (1983).
22. D. Dubbeldam, A. Torres-Knoop and K. S. Walton, *Mol. Simul.*, **39**, 1253 (2013).
23. M. MG, Monte Carlo for complex chemical systems (MCCCS) towhee, version 6.2.12. (2010).
24. J. J. Potoff and J. I. Siepmann, *AIChE J.*, **47**, 1676 (2013).
25. H. J. C. Berendsen, J. R. Grigera and T. P. Straatsma, *J. Phys. Chem.*, **91**, 6269 (1987).
26. L. Zhang and J. I. Siepmann, *Theor. Chem. Acc.*, **115**, 391 (2006).
27. D. Frenkel and B. Smit, Understanding Molecular Simulation From Algorithms to Applications, Academic Press, San Diego (1996).
28. K. A. Northcott, K. Miyakawa, S. Oshima, Y. Komatsu, J. M. Perera and G. W. Stevens, *Chem. Eng. J.*, **157**, 25 (2010).
29. S. Oshima, J. M. Perera, K. A. Northcott, H. Kokusen, G. W. Stevens and Y. Komatsu, *Sep. Sci. Technol.*, **41**, 1635 (2006).
30. Y. N. Xu and W. Y. Ching, *Phys. Rev. B: Condens. Matter*, **44**, 11048 (1991).
31. T. J. H. Vlugt, E. Garcia-Perez, D. Dubbeldam, S. Ban and S. Calero, *J. Chem. Theory Comput.*, **4**, 1107 (2008).
32. A. Poursaeidesfahani, A. Torres-Knoop, M. Rigutto, N. Nair, D. Dubbeldam and T. J. H. Vlugt, *J. Phys. Chem. C*, **120**, 1727 (2016).
33. S. Zhou, C. Guo, Z. Wu, M. Wang, Z. Wang, S. Wei, S. Li and X. Lu, *Appl. Surf. Sci.*, **410**, 259 (2017).
34. B. Yuan, X. Wu, Y. Chen, J. Huang, H. Luo and S. Deng, *Environ. Sci. Technol.*, **47**, 5474 (2013).
35. Q. Yang, C. Xue, C. Zhong and J.-F. Chen, *AIChE J.*, **53**, 2832 (2007).
36. H. Wang, Y. Duan, Y. Li, Y. Xue and M. Liu, *Chem. Eng. J.*, **300**, 230 (2016).
37. E. Di Biase and L. Sarkisov, *Carbon*, **94**, 27 (2015).